Chapter 2

Role of target thickness in proton acceleration from mass-limited plasmas

The role played by the target thickness in generating high energetic protons by a circularly polarized laser from mass-limited targets (MLT) has been investigated with the help of three dimensional (3D) particle-in-cell (PIC) simulations. The target front side gets deformed due to hole boring induced by the radiation pressure. This deformation results in a change in the effective angle of incidence which causes the generation of hot electrons via vacuum heating. These hot electrons travel though the target and on reaching the target rear side form sheath fields which accelerates the protons via target normal sheath acceleration (TNSA) mechanism. The hot electrons travel at an angle with the laser axis and hence the divergence of the hot electron flow increases on increasing the target thickness which can affect the beam collimation. It is observed that the radiation pressure accelerated protons travel across the rear side and the collimation of these protons gets degraded due to the involvement of TNSA process. The transverse hot electron recirculation effects get suppressed and the proton beam collimation increases on decreasing target thickness as radiation pressure acceleration (RPA) starts dominating the acceleration process.

2.1   Background of the study

The role of laser and plasma target parameters on efficient ion acceleration has been investigated experimentally since the last few years. Experimental observations report that the target thickness influences the acceleration. Mackinnon et al. [1] have reported in their experimental observations that the transverse spreading of hot electrons gets reduced on decreasing target thickness which results in a higher rear surface charge density. Kaluza et al. [2] have reported the effect of laser prepulse on proton acceleration from thin Al foils of different thicknesses and have observed that the energy gained by the protons is maximum at an optimum target thickness. Neely et al. [3] have observed that the refluxing and concentration of hot electrons occur within a small volume as the foil thickness is decreased which generates strong electric field and increases the conversion efficiency from laser energy into protons resulting an increase in the maximum proton energy. Recently, the use of mass-limited targets (MLT) has gained a lot of importance in producing high energetic ions due to enhanced acceleration efficiency and increased ion energy as observed both theoretically [4, 5] and experimentally [6, 7]. These targets are in the intermediate regime between atomic clusters and solid foils such as small metal discs or water droplets which have their lateral dimensions comparable to the focal spot size of the laser pulse. In case of soild foils, the hot electrons start spreading towards the transverse directions which increases the transverse dimensions of the sheath formed at the rear side and the sheath size becomes more than the laser spot size. This causes a reduction of maximum energy gained by the ions. In case of MLT, the spreading of hot electrons get reduced to a considerable extent due to low transverse dimensions which result in a more localized and stronger sheath formation and hence enhanced ion energies. Further, when the transverse target dimensions are comparable to the laser spot diameter, the laser may get diffracted and irradiate the points in the target which are not exposed to the laser. The laser electric field is thus able to pull out electrons into vacuum from the target rear side which in turn enhances the sheath field and hence improves the acceleration process. Kluge et al. [8] have shown that the ion energy get enhanced significantly for MLT with diameter below the laser focal spot size. They have observed that as the target diameter is decreased, the hot electrons circulating in the foil drift towards the lateral margins. The hot electrons

which exit the foil are pulled back by the restoring force set up by the ions and they enter the interaction region where they get a chance to be accelerated again. But, as the target diameter is further decreased and becomes comparable to the laser spot size, the recirculations increase and the electrons are heated continuously as they are confined to the focal spot by the electrostatic attraction of the inert target ions. Sokollik et al. [7] have reported an experimental observation on laser-driven ion acceleration from fully isolated, MLT of diameter around 8 μm. They have also used the results of two dimensional (2D) particle-in-cell (PIC) and hydro-code simulations to show that the pre-plasma at both the front and rear sides of the target strongly affect the efficiency of ion acceleration. Andreev et al. [9] have reported that a hemi-sphere foil segment serves as the optimal shape for stable maximum proton acceleration and the optimal diameter of laser beam is about the target diameter for maximal ion energy at minimal geometrical losses. Fujioka et al. [10] have reported that laser-produced mass-limited Sn plasmas can minimize the amount of debris and can enhance the extreme ultraviolet (EUV) emission. The present literature reveals that most of the experiments and simulations on ion acceleration from MLT are done by p-polarized lasers and the acceleration mechanism is mainly the target normal sheath acceleration (TNSA) process with an increased efficiency due to target geometrical effects. However, Heing et al. [11] have reported experimental observations of ion beams accelerated from MLT by a p-polarized laser and they have confirmed their experimental results via. three dimensional (3D) particle-in-cell (PIC) simulations that the ions are accelerated by a converging shock induced by the radiation pressure. Hence, besides TNSA process, the radiation pressure acceleration (RPA) mechanism may also play an important role in the acceleration from MLT. Circularly polarized lasers are found to be more efficient in accelerating ions as there is no oscillating component in the ponderomotive force and hence the electrons can be steadily pushed forward. Hence, circularly polarized lasers can be considered to be a better candidate to induce the effect of RPA. Circulalrly polarized lasers may induce RPA effects in MLT similar to that as observed in case of solid foils.

In the present work we investigate the role of target thickness in proton acceleration from mass-limited plasma targets by an intense short-pulse circularly polarized laser with the help of 3D-PIC simulation using the code Picpsi-3D [12]. Simulations

have been done using MLT of varying thicknesses. Our main aim is to study the detail insight of the processes which occur during the transition from the RPA regime to the TNSA regime and to point out its role in the quality of the proton beam which may be decided by the transverse and axial acceleration as shown in our simulation results. The transverse acceleration degrade the proton beam quality and hence reduce the beam energy. On decreasing the target thickness, it is observed that the transverse acceleration gets reduced and the protons get accelerated more along the axis which may be due to the dominant effect of radiation pressure.

2.2 3D-PIC Simulation Model

The simulations have been done for four different cases using targets of different thicknesses such as 8, 3, 2 and 1 μm. A circularly polarized laser propagating along Z direction of wavelength $\lambda = 1$ μm, normalized electric field amplitude $a_0 (= eE_0/m_e\omega c) \approx$ 10 which corresponds to an intensity of 1.36×10^{20} W/cm^2, pulse duration $\tau = 20$ fs (FWHM) is incident on a plasma target of density 1.15×10^{22} cm^{-3} (10.32 n_c). Here, $n_c = m_e\omega^2/4\pi e^2$ is the critical density where e and m_e are the charge and
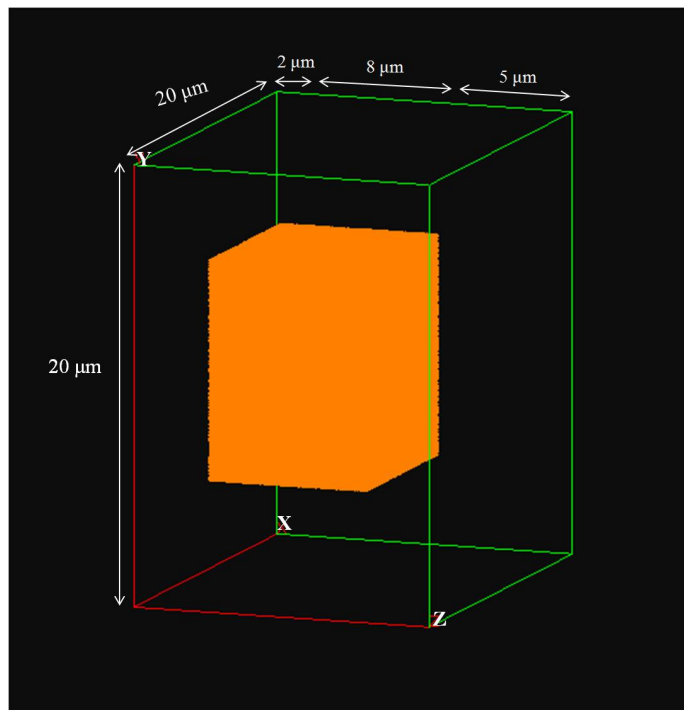

Fig. 2.1: 3D-PIC geometry of the simulation box.

mass of an electron respectively, ω is the laser frequency, E_0 is the laser electric field

amplitude and c is the speed of light. The electron plasma frequency is given as $\omega_{pe} = \sqrt{4\pi n_e e^2/m_e}$ where n_e is the electron plasma density. The spot size of the laser pulse is 3 μm (FWHM) and the laser period T_0 is 3.3 fs. A simulation box of dimensions 20 μm $\times$ 20 μm $\times$ 15 μm consisting of 200 $\times$ 200 $\times$ 150 cells has been used. The plasma slab of height and width 10 μm and thickness 8 μm is sharply edged and is located at a distance of 2 μm from the left boundary of the simulation box as shown in Fig. 2.1. A vacuum gap of 5 μm across the rear side of target is maintained in all the four different cases. Absorbing boundary conditions have been incorporated along all the three directions. The simulations are done with 50 macroparticles per cell. The ions considered in these simulations are protons with mass $m_i = 1836\ m_e$. The plasma is initially assumed to be cold with $T_e = T_i = 0$ where T_e and T_i are the electron and ion temperature respectively.

2.3 Results and Discussion

As the laser intensity is relativistic, the laser may penetrate the classically overdense plasma slab due to relativistically induced transparency [13–15]. The quiver motion of the electrons become relativistic which increases their mass by the Lorentz factor, $\gamma = \sqrt{1 + a_0^2/2}$. The cold electron plasma frequency thus gets modified as $\omega_{pe}^{\gamma} = \sqrt{4\pi n_e e^2/m_e \gamma}$ which becomes less than the laser frequency, ω for $a_0^2 \gg 1$. The effective dielectric constant then makes it possible for the laser pulse to get transmitted through the plasma slab. For the chosen set of laser and plasma parameters, we have $n_e \approx \gamma n_c$ which makes the target partially transparent to the incoming laser pulse. Besides relativistically induced transparency, the RPA induced instabilities may also contribute towards transparency and electron heating inside the plasma. The motion of the laser piston through the plasma can be observed clearly form Fig. 2.2 (a), (b) and (c) which shows the ion density distribution at the central YZ plane at different times 37.63 T_0, 54.47 T_0 and 104 T_0 respectively for the target of thickness 8μm. Fig. 2.3 (a) shows the electrostatic field of the double layer at time 31.69 T_0. The radiation pressure accelerates the protons from the front side of the target. Due to radiation pressure, the front surface of the target is pushed inward and it gets deformed like a cone shape due to the transverse Gaussian shape of the laser pulse as
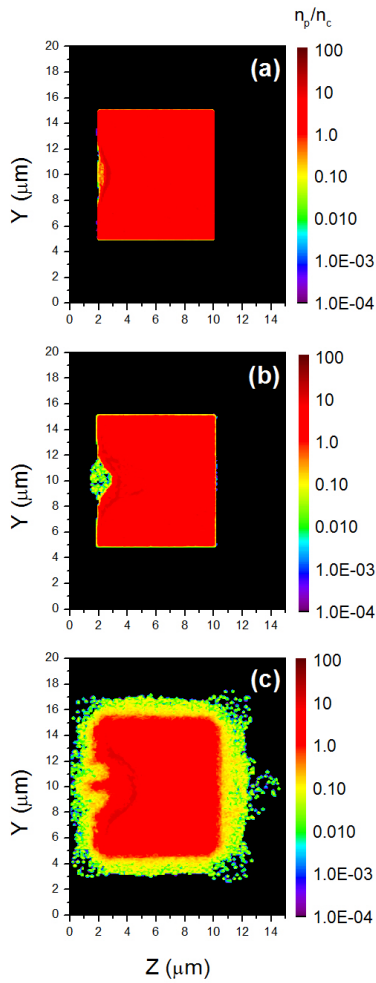
Fig. 2.2: Proton density distribution in the central YZ plane (X = 10 μm) for the target of thickness 8 μm at time (a) 37.63 T_0, (b) 54.47 T_0 and (c) 104 T_0. The proton density n_p is normalized by the critical density $n_c = 1.12 \times 10^{21}$ cm^{-3}.
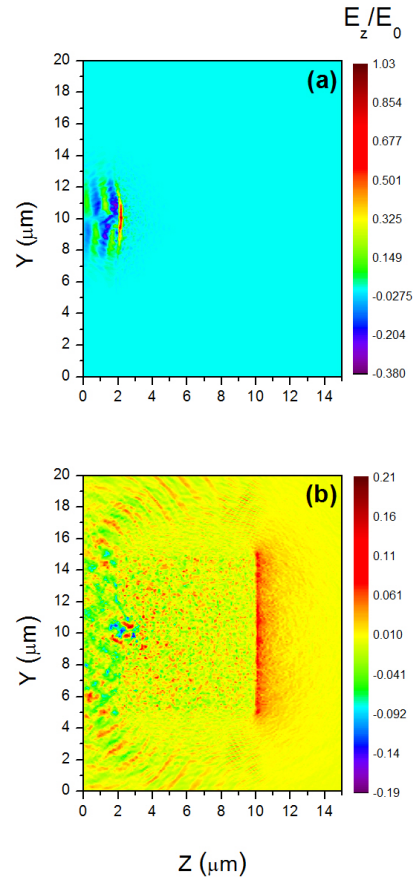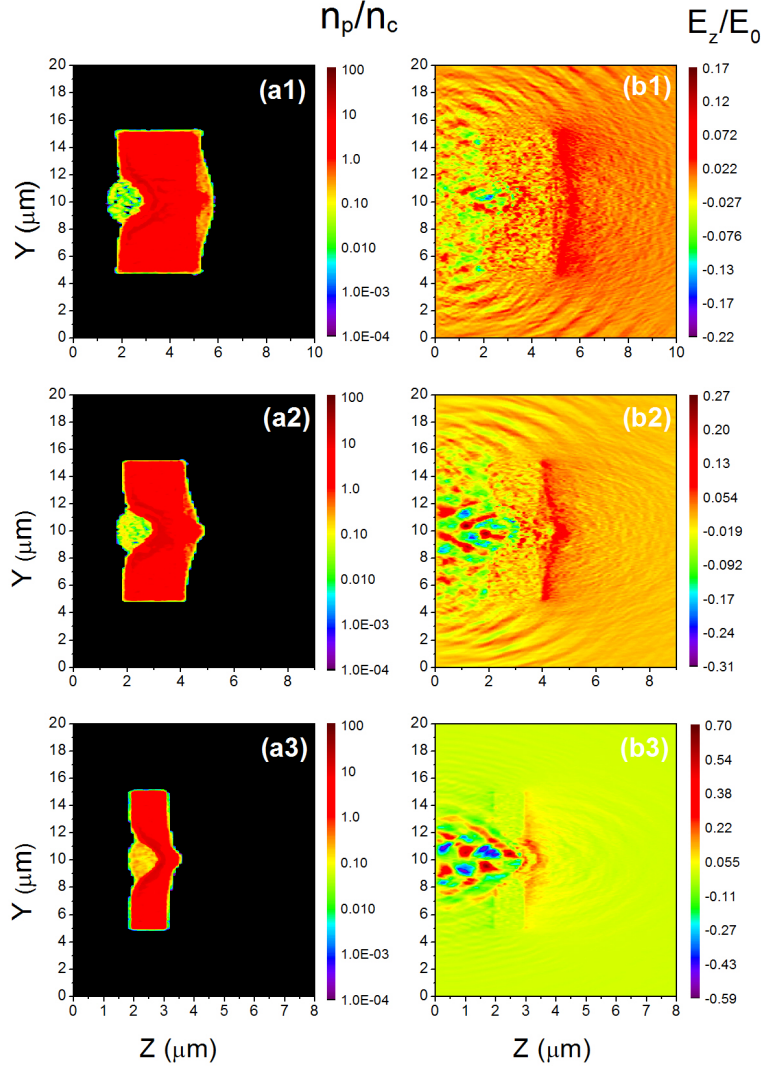
Fig. 2.3: Longitudinal electric field E_z normalized by the laser electric field E_0 in the central YZ plane (X = 10 μm) for the target of thickness 8 μm at time (a) 31.69 T_0 and (b) 54.47 T_0.

observed in Fig. 2.2 (b). The effective laser pulse incidence becomes oblique at the edges of the laser focal spot. The laser pulse then starts getting reflected from one edge of the cone and is incident on the other edge [16]. This continues and the piston gets degraded which results in the formation of several clumps through which the laser pulse can penetrate. Pegoraro and Bulanov [17] showed that Rayleigh-Taylor (RT) instabilities may result in making the foil transparent as they are accelerated to relativistic velocities. The effects of such instabilities can be reduced by a proper tailoring of the laser pulse. Such effects are not observed in 1D simulations due to absence of multidimensional effects. These transverse effects broaden the energy

spectrum. Due to effective oblique incidence, a normal electric field component arises from the tilt of the plasma boundary with respect to the laser propagation direction. The electric field component normal to the edges of the cone shaped deformed surface would lead to electron heating via. "vacuum heating" [18] process. Chen et al. [19] have mentioned that with effective oblique angle of incidence at the deformed surface, the electrons start getting heated by vacuum heating process. The hot electrons disperse around the target and broaden the energy spectrum. They have investigated that the monoenergetic nature of the energy spectrum can be obtained by using super-Gaussian laser pulses. Gaussian pulses have a sharp transverse intensity profile which bends the plasma surface whereas super-gaussian or flat top pulses have a smooth and flat intensity profile which can push the piston more effectively with minimal deformation and hence would reduce the effects of vacuum heating. Brantov and Bychenkov [20] have reported that the monoenergetic nature as well as the maximum energy of proton beams accelerated from MLT improve significantly on using super-Gaussian laser pulses. In our case, since we have used a laser pulse with transverse Gaussian profile, the target becomes transparent and it also causes the vacuum heating of electrons at the deformed plasma region.

The highly energetic electrons generated at the deformed front plasma surface then gets transported through the target which eventually reaches the target rear side and results in the formation of a sheath field which accelerates the protons from the target rear side via TNSA mechanism. For larger target thickness, the hot electrons would get more diverged from the laser axis as they travel long distance through the target which would cause the transverse expansion of the sheath formed at the rear side. However, the hot electrons generated at the tip of the cone would be much more energetic as the laser intensity is highest at this point and they would travel along the laser axis. Hence, the electrostatic field of the electron sheath at the target rear side would be strongest on the axis rather than along the transverse directions. The electrostatic field of the electron sheath at time 54.47 T_0 is shown in Fig. 2.3 (b) which rises very sharply at the rear side of the target. Due to limited transverse size of the target, the hot electrons escape from the lateral edges along the transverse directions and may re-enter the interaction regime due to the restoring force set up by the protons. The oscillating nature of the longitudinal electric field

diverging along transverse directions from the interaction region may be due to the hot electron recirculations as shown in Fig. 2.3 (b). These transverse hot electron recirculations may also contribute towards the increase in transverse expansion of the sheath and hence would result in the divergence of the proton beam.


Fig. 2.4: Proton density distribution (a1-a3) and longitudinal electric field E_z (b1-b3) in the central YZ plane (X = 10 μm) for targets of thicknesses 3, 2 and 1 μm at times 54.47 T_0, 49.52 T_0 and 41.60 T_0 respectively. The proton density n_p is normalized by the critical density $n_c = 1.12 \times 10^{21}$ cm^{-3} and the longitudinal electric field E_z is normalized by the laser electric field E_0.

The simulation is repeated by decreasing the thickness of the same target to 3 μm. Fig. 2.4 (a1) and (b1) shows the proton density distribution and the electrostatic field at time 54.47 T_0 respectively. The simulation is repeated again by decreasing the thickness to 2 μm. The on axis acceleration of protons is more in this case as

observed in Fig. 2.4 (a2) and (b2). On decreasing the target thickness further to 1 μm, it is observed that hole boring reaches the rear side of the target as shown in Fig. 2.4 (a3) and (b3). The transverse hot electron recirculations are observed to be least in case of the target of thickness 1 μm as RPA starts dominating the acceleration process. The electron distribution across the rear side is plotted in Fig. 2.5 (a), (b), (c) and (d) for targets of thicknesses 8, 3, 2 and 1 μm respectively. It is observed that
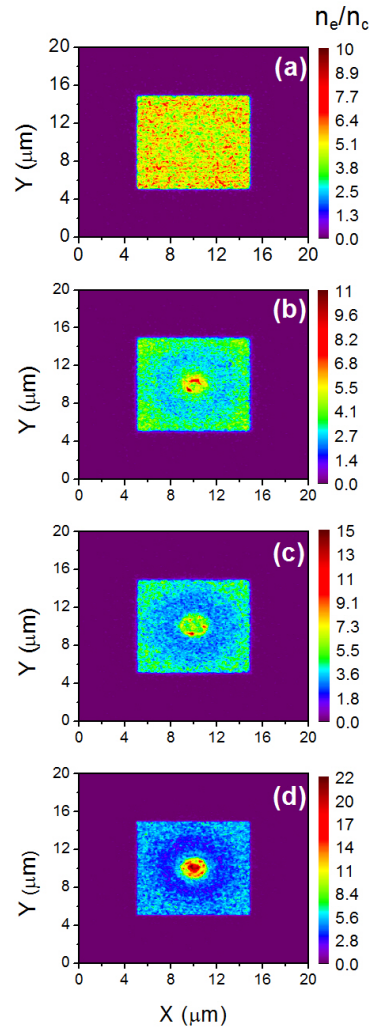
Fig. 2.5: Electron density distribution in the XY plane at the rear edge of the target of thickness (a) 8 μm at Z = 10 μm and time 54.47 T_0, (b) 3 μm at Z = 5 μm and time 54.47 T_0, (c) 2 μm at Z = 4 μm and time 49.52 T_0 and (c) 1 μm at Z = 3 μm and time 41.60 T_0. The electron density n_e is normalized by the critical density $n_c = 1.12 \times 10^{21}$ cm^{-3}.

the flow of energetic electrons towards the rear side along the axial and transverse directions is almost equal in case of the target of thickness 8 μm. On the other hand, electron density across the rear side is higher on the axis as the target thickness is reduced to 3 μm and much higher when further reduced to 2 μm and then to 1 μm.

Fig. 2.6 (a1-a4) and (b1-b4) represents the normalized axial momentum $p_z/m_i c$ phase space and transverse momentum $p_y/m_i c$ phase space for targets of thickness 8, 3, 2 and 1 μm respectively. In case of 8 μm target, it can be clearly observed from Fig. 2.6 (a1) that the protons which get accelerated from the target front surface by the radiation pressure are much more energetic as compared to those which get accelerated from the back surface by the TNSA mechanism. Thus, the radiation
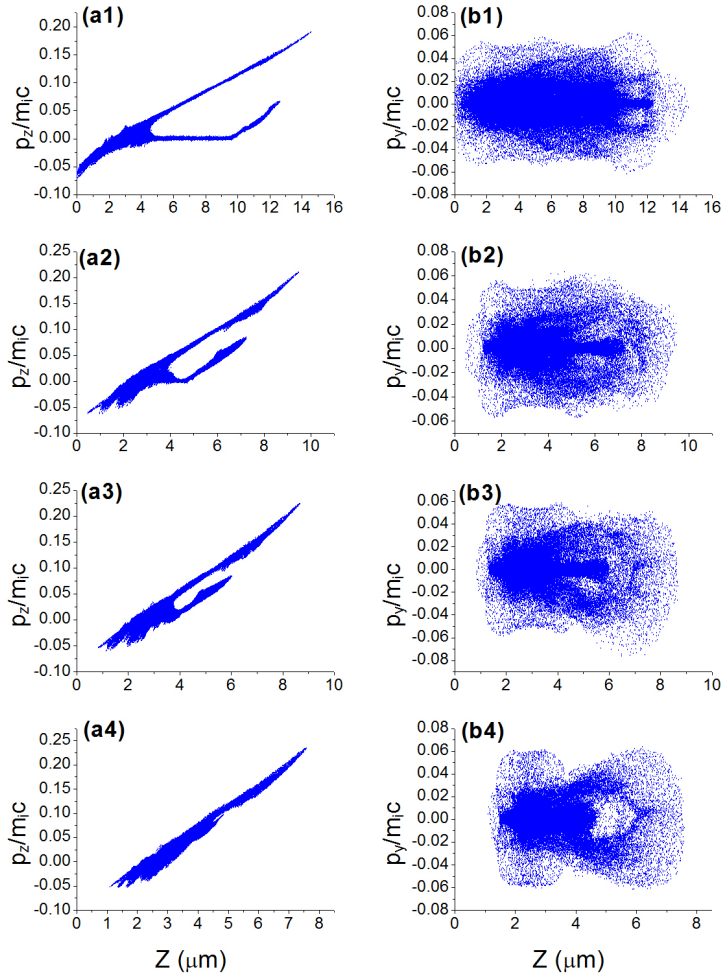
Fig. 2.6: Normalized axial momentum $p_z/m_i c$ (a1-a4) and transverse momentum $p_y/m_i c$ (b1-b4) phase space for targets of thicknesses 8, 3, 2 and 1 μm at times 104 T_0, 74.28 T_0, 68.34 T_0 and 61.41 T_0 respectively.

pressure accelerated protons travel through the target and on reaching the rear side, get accelerated by the sheath field. Plasma expansion occurs along all the three directions which degrades the energetic proton beam quality. Comparing Fig. 2.6 (a1) and (b1), it can be observed that the radiation pressure accelerated protons

from the target front surface which travel through the target and eventually reach the rear side has higher axial momentum as compared to those which get accelerated from the rear side by the sheath field. It can also be observed that the axial and transverse momentum of the protons accelerated from the target rear side by TNSA mechanism are nearly same. It can be observed that the protons which are accelerated along the axis as shown in Fig. 2.2 (c) are the ones which are accelerated mainly by the radiation pressure. On comparing Figs. 2.6 (b1-b4), it can be observed that
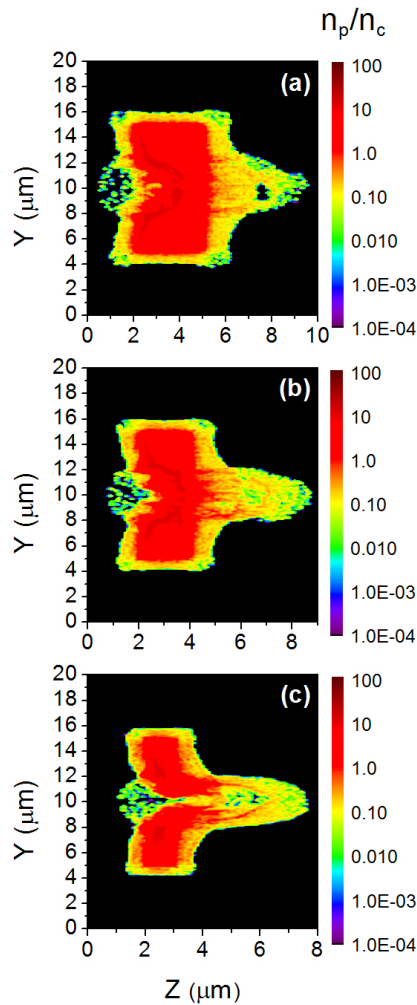
Fig. 2.7: Proton density distribution in the central YZ plane (X = 10 μm) when the protons gain maximum energy for the target of thickness (a) 3 μm at time 74.28 T_0, (b) 2 μm at time 68.34 T_0 and (c) 1 μm at time 61.41 T_0. The proton density n_p is normalized by the critical density $n_c = 1.12 \times 10^{21}$ cm^{-3}.

though the values of transverse momentum is almost same for all considered targets, but there are highest number of energetic protons along higher values of transverse momentum in case of 8 μm target. The number of energetic protons across the target

rear side tends to be more towards lower values of transverse momentum as the target thickness is decreased upto 1 μm. Thus, it can be concluded that RPA induced by the a circularly polarized laser provides better collimation than TNSA. Fig. 2.7 shows the proton density distribution at times when the proton energy is maximum. It can be observed from Fig. 2.7 that as we go on decreasing the thickness of the target up to 1 μm, the energetic proton beam gets more and more collimated as RPA starts dominating the acceleration process.
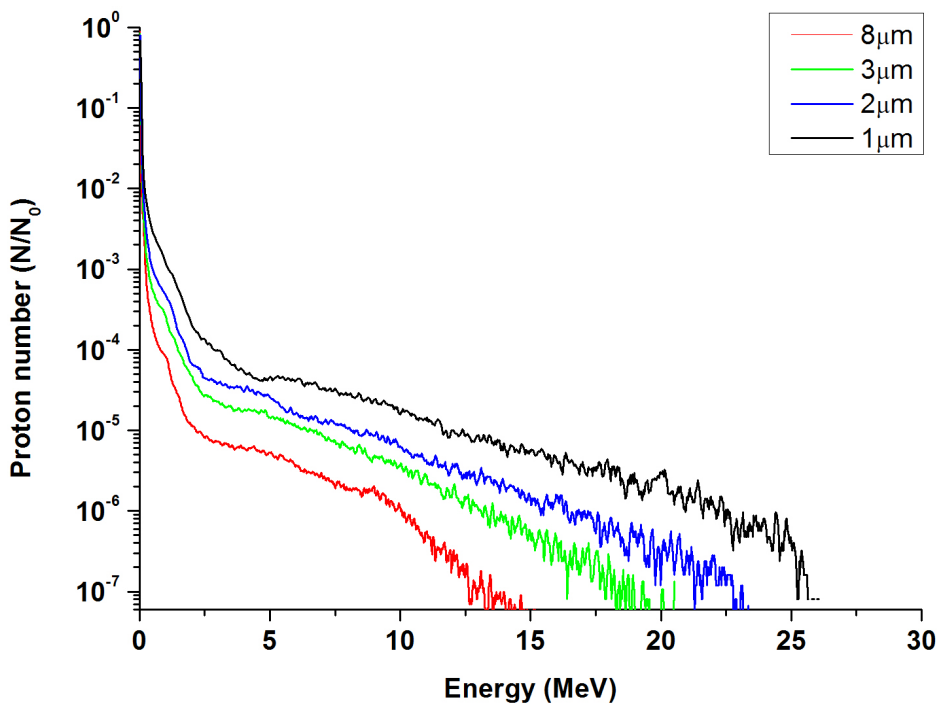
Fig. 2.8: Proton energy spectrum for the target of thickness 8 μm (red solid) at time 104 T_0, 3 μm (green solid) at time 74.28 T_0, 2 μm (blue solid) at time 68.34 T_0 and 1 μm (black solid) at time 61.41 T_0. The proton number N is normalized by the total number of protons N_0 in each case.

Fig. 2.8 represents the proton energy spectrum for all the four targets. It is found that the proton energy increases as the target thickness is decreased. Though we have observed that RPA dominates the acceleration process producing well collimated high energetic proton beams, we have not observed any quasi-monoenergetic character in the energy spectra. Though it is well known to us that TNSA produces collimated energetic proton beams, but the collimation is comparatively less than the protons accelerated by RPA due to a circularly polarized laser. The energy spectrum gets

broadened and the quasi-monoenergetic character gets diluted due to the involvement of TNSA process. A nearly quasi-monoenergetic peak at ≈ 8 MeV can be observed at an early time 37.63 T_0 which gets deteriorated at a later time 104 T_0 when the TNSA starts participating in the acceleration process as shown in Fig. 2.9. For the
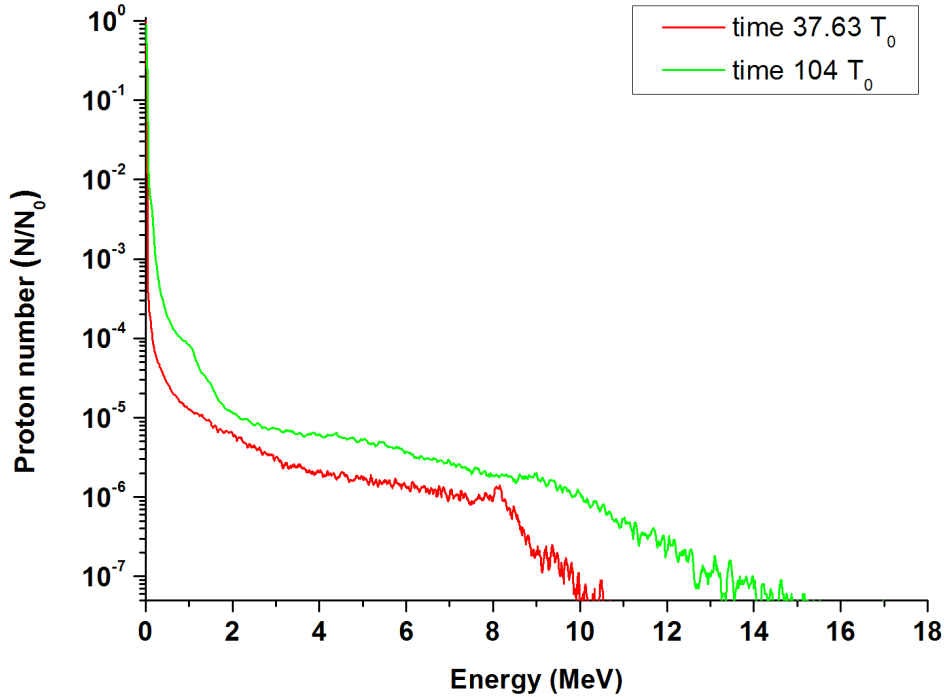

Fig. 2.9: Proton energy spectrum for the target of thickness 8 μm at time 37.63 T_0 (red solid) and 104 T_0 (green solid). The proton number N is normalized by the total number of protons N_0.

range of target thickness presented here, we have observed an increase in maximum proton energy as the target thickness is decreased up to 1 μm. On further decreasing the target thickness upto 0.2 μm, and it is found that the proton energy is maximum for an optimum thickness of 0.5 μm as shown in Fig. 2.10.

In order to have a better understanding of the effect of laser polarization on proton acceleration from mass-limited targets, we repeated the simulation for the target of thickness 2 μm with a p-polarized laser. As observed in Fig. 2.11 (a), most of the protons are accelerated from the target rear side via. TNSA process. Though the accelerated protons are fairly collimated but the collimation is not good enough as compared with the protons accelerated by the circularly polarized laser. The transverse expansion of the target is more in this case due to increased transverse

hot electron recirculation. This transverse motion of the electrons and protons is mainly due to the oscillating $\vec{J} \times \vec{B}$ component of the ponderomotive force of the p-polarized laser which heats bulk of the target completely. This volumic heating causes plasma expansion and reduces the effect of radiation pressure which causes the broadening of energy spectrum and result in poor proton beam collimation. In this case, TNSA dominates the acceleration process and most of the protons are accelerated from the target rear side as shown in Fig. 2.11 (b). In case of a circularly
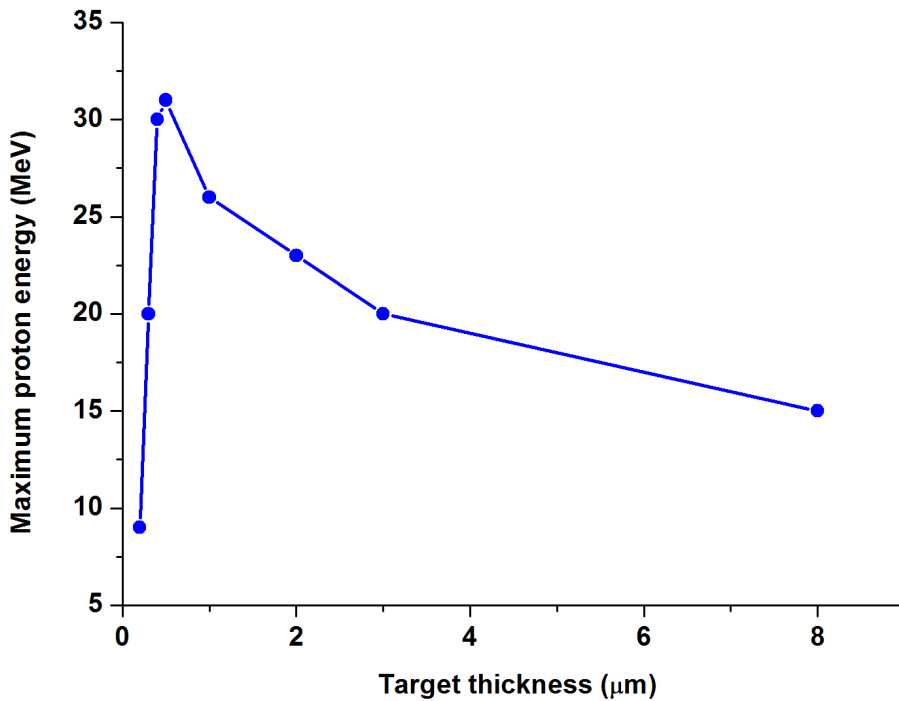
Fig. 2.10: Variation of maximum proton energy with target thickness.

polarized laser pulse, the plasma particles are pushed steadily in the forward direction due to the absence of the oscillatory component which reduces the volumic plasma heating and the plasma expansion is considerably less as shown in Fig. 2.7 (b). The simulation by a p-polarized laser is repeated for the target of optimum thickness 0.5 μm. The maximum energy gained by the protons is comparatively less than that produced by the circularly polarized laser as shown in Fig. 2.12. Willingale et al. [21] have observed the front surface ion acceleration from plasmas with densities $n_e = 3n_c - 15n_c$ but the energy is always less than the rear surface accelerated ions due to efficiency of hot electron generation. However, in our case, the front surface

ion acceleration is higher than the rear surface on using a circularly polarized laser. Hence, it can be concluded that a circularly polarized laser can accelerate protons up to high energies with good collimation from mass-limited targets due to the dominant effect of radiation pressure.
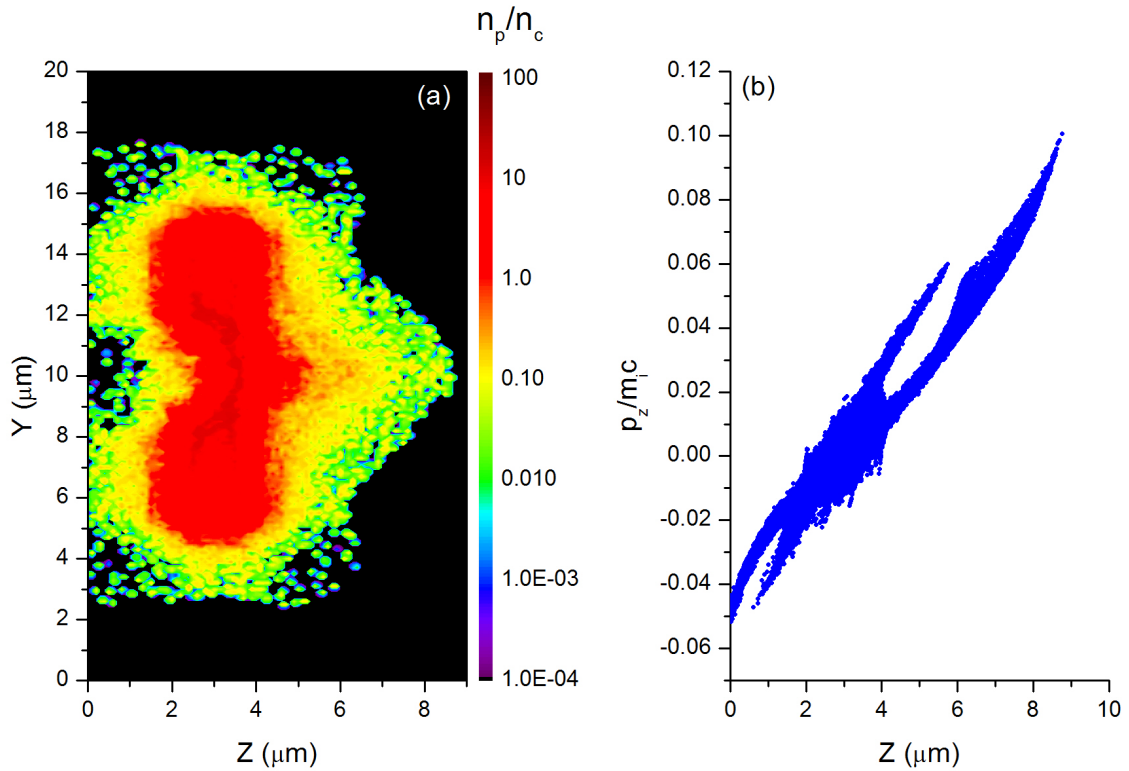

Fig. 2.11: (a) Proton density distribution in the central YZ plane (X = 10 μm) and (b) Axial momentum $p_z/m_i c$ phase space when the protons gain maximum energy for the target of thickness 2 μm by a p-polarized laser at time 98.05 T_0. The proton density n_p is normalized by the critical density $n_c = 1.12 \times 10^{21}$ cm^{-3}.

2.4 Conclusion

The role played by the target thickness in generating high energetic protons from near-critical mass-limited plasma targets by an ultraintense short pulse circularly polarized laser has been investigated with the help of 3D-PIC simulations. The simulations have been done using targets of thicknesses 8, 3, 2 and 1 μm. The conclusions drawn from the above discussions can be summarized as follows :

   i) Protons get accelerated more effectively from the target front surface due to the
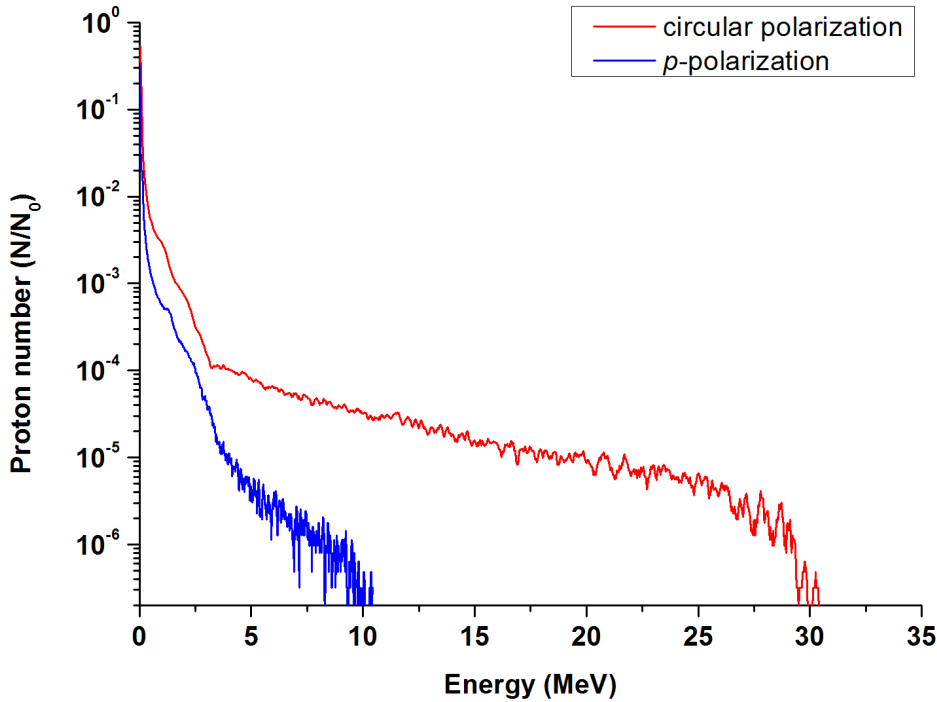
Fig. 2.12: Proton energy spectrum for the target of optimum thickness 0.5 μm by a circularly polarized laser (red solid) at time 57.44 T_0 and a p-polarized laser (blue solid) at time 73.29 T_0. The proton number N is normalized by the total number of protons N_0.

radiation pressure of a circularly polarized laser. The front surface accelerated protons are more energetic and collimated than the ones which are accelerated by the TNSA mechanism from the target rear side.

ii) The radiation pressure accelerated protons are highly energetic and hence travel much faster through the target and reach the target rear side as the target thickness is decreased. Thus, RPA dominates the acceleration process on decreasing target thickness which leads to an increase in maximum proton energy and beam collimation.

iii) The use of a circularly polarized laser reduces volumic heating and also prevents the effect of transverse hot electron recirculations to a considerable extent which improves the energetic proton beam collimation.

iv) The maximum proton energy as well as the number of accelerated protons increases on decreasing target thickness. However, the monoenergetic character

is not observed in the energy spectrum as the monoenergetic nature of RPA is diluted due to multidimensional effects.

v) For same values of laser intensity and target thickness, TNSA mechanism dominates over RPA for a p-polarized laser while the reverse happens for a circularly polarized laser.

vi) The proton energy obtained is found to be maximum for the target of an optimum thickness of 0.5 μm.

Bibliography

[1] Mackinnon, A. J., Sentoku, Y., Patel, P. K., Price, D. W., Hatchett, S., Key, M. H., Andersen, C., Snavely, R., and Freeman, R. R. Enhancement of proton acceleration by hot-electron recirculation in thin foils irradiated by ultraintense laser pulses. *Phys. Rev. Lett.*, 88:215006, 2002.

[2] Kaluza, M., Schreiber, J., Santala, M. I. K., Tsakiris, G. D., Eidmann, K., Meyer-ter Vehn, J., and Witte, K. J. Influence of the laser prepulse on proton acceleration in thin-foil experiments. *Phys. Rev. Lett.*, 93:045003, 2004.

[3] Neely, D., Foster, P., Robinson, A., Lindau, F., Lundh, O., Persson, A., Wahlstrm, C.-G., and McKenna, P. Enhanced proton beams from ultrathin targets driven by high contrast laser pulses. *Applied Physics Letters*, 89(2): 021502, 2006.

[4] Pšikal, J., Limpouch, J., Kawata, S., and Andreev, A. A. Pic simulations of femtosecond interactions with mass-limited targets. *Czechoslovak Journal of Physics*, 56(2):B515–B521, 2006.

[5] Limpouch, J., Psikal, J., Andreev, A., Platonov, K. Y., and Kawata, S. Enhanced laser ion acceleration from mass-limited targets. *Laser and Particle Beams*, 26(2):225234, 2008.

[6] Sokollik, T., Schnürer, M., Steinke, S., Nickles, P. V., Sandner, W., Amin, M., Toncian, T., Willi, O., and Andreev, A. A. Directional laser-driven ion acceleration from microspheres. *Phys. Rev. Lett.*, 103:135003, 2009.

[7] Sokollik, T., Paasch-Colberg, T., Gorling, K., Eichmann, U., Schnrer, M., Steinke, S., Nickles, P. V., Andreev, A., and Sandner, W. Laser-driven ion acceleration using isolated mass-limited spheres. *New Journal of Physics*, 12 (11):113013, 2010.

[8] Kluge, T., Enghardt, W., Kraft, S. D., Schramm, U., Zeil, K., Cowan, T. E., and Bussmann, M. Enhanced laser ion acceleration from mass-limited foils. *Physics of Plasmas*, 17(12):123103, 2010.

[9] Andreev, A. A., Limpouch, J., Psikal, J., Platonov, K. Y., and Tikhonchuk, V. T. Laser ion acceleration in a mass limited targets. *The European Physical Journal Special Topics*, 175(1):123–126, 2009.

[10] Fujioka, S., Nishimura, H., Nishihara, K., Murakami, M., Kang, Y.-G., Gu, Q., Nagai, K., Norimatsu, T., Miyanaga, N., Izawa, Y., Mima, K., Shimada, Y., Sunahara, A., and Furukawa, H. Properties of ion debris emitted from laser-produced mass-limited tin plasmas for extreme ultraviolet light source applications. *Applied Physics Letters*, 87(24):241503, 2005.

[11] Henig, A., Kiefer, D., Geissler, M., Rykovanov, S. G., Ramis, R., Hörlein, R., Osterhoff, J., Major, Z., Veisz, L., Karsch, S., Krausz, F., Habs, D., and Schreiber, J. Laser-driven shock acceleration of ion beams from spherical mass-limited targets. *Phys. Rev. Lett.*, 102:095002, 2009.

[12] Upadhyay, A., Patel, K., Rao, B. S., Naik, P. A., and Gupta, P. D. Three-dimensional simulation of laser–plasma-based electron acceleration. *Pramana*, 78(4):613–623, 2012.

[13] Akhiezer, A. and Polovin, R. Theory of wave motion of an electron plasma. *Soviet Phys. JETP*, Vol: 3, 1956.

[14] Kaw, P. and Dawson, J. Relativistic nonlinear propagation of laser beams in cold overdense plasmas. *The Physics of Fluids*, 13(2):472–481, 1970.

[15] Max, C. and Perkins, F. Strong electromagnetic waves in overdense plasmas. *Phys. Rev. Lett.*, 27:1342–1345, 1971.

[16] Macchi, A., Veghini, S., Liseykina, T. V., and Pegoraro, F. Radiation pressure acceleration of ultrathin foils. *New Journal of Physics*, 12(4):045013, 2010.

[17] Pegoraro, F. and Bulanov, S. V. Photon bubbles and ion acceleration in a plasma dominated by the radiation pressure of an electromagnetic pulse. *Phys. Rev. Lett.*, 99:065002, 2007.

[18] Brunel, F. Not-so-resonant, resonant absorption. *Phys. Rev. Lett.*, 59:52–55, 1987.

[19] Chen, M., Pukhov, A., Sheng, Z. M., and Yan, X. Q. Laser mode effects on the ion acceleration during circularly polarized laser pulse interaction with foil targets. *Physics of Plasmas*, 15(11):113103, 2008.

[20] Brantov, A. V. and Bychenkov, V. Y. Monoenergetic proton beams from mass-limited targets irradiated by ultrashort laser pulses. *Plasma Physics Reports*, 36 (3):256–262, 2010.

[21] Willingale, L., Nagel, S. R., Thomas, A. G. R., Bellei, C., Clarke, R. J., Dangor, A. E., Heathcote, R., Kaluza, M. C., Kamperidis, C., Kneip, S., Krushelnick, K., Lopes, N., Mangles, S. P. D., Nazarov, W., Nilson, P. M., and Najmudin, Z. Characterization of high-intensity laser propagation in the relativistic transparent regime through measurements of energetic proton beams. *Phys. Rev. Lett.*, 102:125002, 2009.